



Quantifying urban heat island intensity and its physical mechanism using WRF/UCM

Huidong Li^a, Yuyu Zhou^b, Xun Wang^a, Xu Zhou^c, Huiwen Zhang^a, Sahar Sodoudi^{a,*}

^a Institute of Meteorology, Freie Universität Berlin, Berlin, Germany

^b Department of Geological and Atmospheric Sciences, Iowa State University, Ames, IA, USA

^c Key Laboratory of Tibetan Environment Changes and Land Surface Processes, Institute of Tibetan Plateau Research, Chinese Academy of Sciences, Beijing, China

HIGHLIGHTS

- High-resolution urban heat island was simulated using WRF/UCM.
- The linear function of simulated air temperature against impervious surface area was used to quantify UHI intensity.
- The physical mechanism of the derived UHI intensity was examined.

GRAPHICAL ABSTRACT

$$\begin{aligned}
 T_s &= FRC_URB \times T_{s(\text{impervious})} + (1 - FRC_URB) \times T_{s(\text{vegetation})} \\
 SH &= FRC_URB \times SH_{(\text{impervious})} + (1 - FRC_URB) \times SH_{(\text{vegetation})} \\
 T_{2m} &= T_s - \frac{SH}{\rho C_{h2m} U_{2m}} \\
 T_{2m} &= FRC_URB \times \left(T_{s(\text{impervious})} - T_{s(\text{vegetation})} - \frac{SH_{(\text{impervious})} - SH_{(\text{vegetation})}}{\rho C_{h2m} U_{2m}} \right) + T_{s(\text{vegetation})} - \frac{SH_{(\text{vegetation})}}{\rho C_{h2m} U_{2m}} \\
 &\quad \text{UHII} \quad \quad \quad T_{2m(\text{vegetation})}
 \end{aligned}$$

ARTICLE INFO

Article history:

Received 5 July 2018

Received in revised form 13 September 2018

Accepted 2 October 2018

Available online 03 October 2018

Editor: Pavlos Kassomenos

Keywords:

Urban heat island intensity

Impervious surface area

Urban parameters

WRF/UCM

Berlin

ABSTRACT

Reliable quantification of urban heat island intensity (UHII) is crucial for the evaluation of extreme heat waves and the related heat stress. As a powerful approach for the study of urban climate, numerical models can simulate urban heat island (UHI) in both high spatial and temporal resolutions. However, accurate quantification of UHII using modelling grid data is still a challenge at present, due to the different criteria for the selection of urban/rural grids. This study simulates the high-resolution UHI in the city of Berlin using the Weather Research and Forecasting Model coupled with Urban Canopy Module. A new method to quantify UHII, which is based on the fitted linear functions of simulated 2-m air temperature (T_{2m}) using the impervious surface area in WRF grids (ISA_{WRF}), was adopted and evaluated. The simulated T_{2m} matches the observations well, with a correlation coefficient of 0.95 ($P < 0.01$) and RMSE of 1.76 °C. The study area shows a strong UHI at nighttime. The simulated nighttime T_{2m} increases with the increase in the ISA_{WRF} . The linear functions of simulated nighttime T_{2m} against ISA_{WRF} are well fitted. The UHII is calculated as the products of the slopes of fitted functions and the largest ISA_{WRF} . The derived UHII shows U-shaped diurnal variations, with high values at nighttime. The difference of simulated surface temperature and sensible heat flux between the impervious surface and the vegetation surface jointly determines the derived UHII. The large difference of surface temperature and the small difference of sensible heat flux between the impervious and the vegetation surface generate the high UHII at nighttime and vice versa during the daytime. The method of ISA_{WRF} -based function of T_{2m} overcomes the problems of traditional methods in arbitrary selecting urban/rural grids. It can be used easily to quantify UHII and to do the comparison study of UHII between different cities.

© 2018 Elsevier B.V. All rights reserved.

* Corresponding author at: Carl-Heinrich-Becker-Weg 6-10, 12165 Berlin, Germany.

E-mail address: sodoudi@zedat.fu-berlin.de (S. Sodoudi).

1. Introduction

The Urban Heat Island (UHI) effect refers to the warmer temperatures in urban areas than in surrounding rural areas, due to urbanization (Rizwan et al., 2008). UHI can strengthen heat waves, increasing the heat load to urban dwellers (Tan et al., 2010). It is projected that rapid urbanization will continue during this century (AAAS, 2016). With more build-up surface being constructed and more people crowding into cities, UHI will become more intense (Yang et al., 2017). Furthermore, climate change will enhance the frequency and intensity of extreme heat waves in the future (e.g. Meehl and Tebaldi, 2004). Urban residents will suffer from a higher risk of heat stress, which has a negative effect on human thermal comfort and heat-related illnesses. The studies on UHI (e.g. spatial and temporal patterns, driving factors, and mitigation strategies) became more important and received a great deal of attention in recent years (Phelan et al., 2015). Among all these topics, accurate quantification of UHI intensity (UHII) is the first step.

Currently, in-situ observation, remote sensing observation, and numerical modelling are the most used approaches for the study of UHI (Mirzaei and Haghighat, 2010). Usually, in-situ observation cannot reflect the spatial pattern of UHI well, due to sparse stations and remote sensing observation is unable to capture the temporal variation of UHI well, due to the low temporal resolution and the disturbance of clouds. Compared to in-situ and remote sensing observations, numerical modelling can be used to study UHI in both high spatial and temporal resolution (San José et al., 2013). Numerical modelling has become a powerful approach for the study of UHI and has been used for the wide studies of UHI, such as investigation of the physical mechanism and drivers of UHI (e.g. H. Li et al., 2017; X. Li et al., 2017), the pre-warning of heat waves (e.g. Zauri et al., 2010), the simulation of future scenarios (e.g. Kusaka et al., 2012), and the evaluations of urbanization effect (e.g. Zhong et al., 2017) and mitigation strategies of UHI (e.g. Jacobs et al., 2018).

However, accurate quantification of UHII using modelling grid data is still a challenge at present, although robust data are available from numerical modelling. In most of the previous studies, the UHII was calculated using the modelling data at selected urban grids and rural grids (e.g. Atkinson, 2003; Hamdi and Schayes, 2008; Salamanca et al., 2012). However, there is no unified criterion for the selections of urban and rural grids (Stewart and Oke, 2012). The grids are selected based on land cover categories (e.g. Zhao et al., 2014; Cao et al., 2016) or impervious surface areas (ISA) (e.g. Imhoff et al., 2010; Zhang et al., 2012). As a result, the derived UHII may vary largely and is not comparable due to the different selection of the grids. Schwarz et al. (2011) calculated UHII in European cities using eleven approaches for the selection of the grids and found that the derived UHII using different grids showed great differences. Different criteria for urban and rural grids make the inter-comparison of UHII among different studies challenging (Stewart, 2011). Additionally, the UHI intensity was defined as the maximum temperature difference between urban and rural areas in a city (e.g. Oke, 1973). This difference cannot be properly represented by local temperature difference between the limited selected grids.

Land use change from natural surface to impervious surface is the major contribution to UHI (Oke, 1982). ISA represents the ratio of impervious surface area in a grid, with a high value in highly-urbanized areas and a low value in rural areas. There is a close relationship between near-surface temperature and ISA in the spatial distribution (e.g. Kottmeier et al., 2007; Zhang et al., 2010). Schatz and Kucharik (2014) concluded that ISA was the primary driver of the spatial variations of air temperature and accounted for 80% of the spatial variations in the daytime and 74% of the spatial variations in the nighttime in Madison, USA, based on observations. Ryu and Baik (2012) also reported the important contribution of imperviousness on the UHI by using a mesoscale atmospheric model. Usually, the near-surface temperature increases with the increase in ISA, presenting a linear trend. Schatz and Kucharik (2014, 2015) and Li et al. (2018a) fitted the linear functions of in-situ observed air temperature and remote sensing land

surface temperature, respectively, using ISA. The slope of fitted functions represented the increase in the temperatures when the surface changed from natural to impervious and was used to calculate UHII. Although the ISA-based function of the near-surface temperature provides a promising method to quantify UHII using grid data. An application and evaluation of this new method in quantifying UHII using modelling grid data is still lacking and needed.

This study attempts to quantify UHII by applying the new method and the modelling data of Weather Research and Forecasting Model coupled with Urban Canopy Module (WRF/UCM), which is a widely used numerical model for the study of urban climate (Chen et al., 2011). The high-resolution UHI was simulated during a clear sky and calm wind period in the city of Berlin. The relationship between the simulated air temperature and the ISA in the WRF grids (ISA_{WRF}) was analyzed for different time periods of the day. The linear functions of the simulated air temperature were fitted against ISA_{WRF} . The temporal variation of the derived UHII was investigated and compared to those using traditional methods. The physical mechanism that controlled the derived UHII in the WRF/UCM was discussed based on the numerical functions of the model. The goal of this study is to (1) evaluate the feasibility of the ISA_{WRF} -based functions of the simulated air temperature in quantifying UHII, (2) investigate the spatial and temporal variations of the simulated UHI in the city of Berlin, and (3) examine the physical mechanism that controls the derived UHII.

2. Study area and methodology

2.1. Study area

The study area is Berlin (52.34°–52.68° N, 13.10°–13.77° E), the capital city of Germany (Fig. 1a). Berlin is located in a temperate maritime climate zone. The mean annual temperature was 9.5 °C and the mean annual precipitation was 591 mm (based on the observation record at the DWD Dahlem station from 1981 to 2010). According to the report 2015 of the Statistical Office of Berlin-Brandenburg, about 3.5 million inhabitants live in this city. Berlin covers an area of around 900 km², with a flat topography (34–122 m, altitude). About 35% of the area is covered by the built-up surface and about 20% of the area is covered by the paving surface of transport and infrastructure (Fig. 1b). The non-urban area is mainly covered by vegetation ecosystems, including forests and farmlands. Berlin's large built-up and paving areas create a microclimate with pronounced UHI effects (Li et al., 2018b).

2.2. Model description and configuration

2.2.1. WRF/UCM model

WRF/UCM version 3.7.1 was employed in this study. WRF is one of the most advanced numerical weather prediction system developed by the National Center for Atmospheric Research, USA. In order to address urban environmental issues, an integrated urban modelling system was developed to couple with the Noah-LSM scheme of WRF (Chen et al., 2011). The UCM used in this study is a single-layer model, which considers the shadowing, reflections, and trapping of radiation, the street orientation and diurnal variation of azimuth angle, surface energy budget of roofs, walls and roads, the wind profile in the canopy layer, and anthropogenic heat emissions (Kusaka et al., 2005). More detailed description of the UCM refers to Kusaka et al. (2001) and Kusaka and Kimura (2004). WRF/UCM is a promising utility for the urban climate related studies and has been widely used in the metropolitan regions of North America (e.g. Los Angeles) (Vahmani and Hogue, 2015), Asia (e.g. Beijing, Tokyo) (Miao et al., 2009; Kusaka et al., 2012) and Europe (e.g. London, Athens, Helsinki, Firenze, Gliwice) (San José et al., 2013; Giannaros et al., 2018).

2.2.2. Domain setup and physical parameterization configuration

Three nested domains with the horizontal grid spacing of 15 km, 3 km, and 1 km were designed, with 119 × 119, 155 × 155 and 111 × 111 grid cells, respectively (Fig. 1a). In the vertical direction, 35 levels

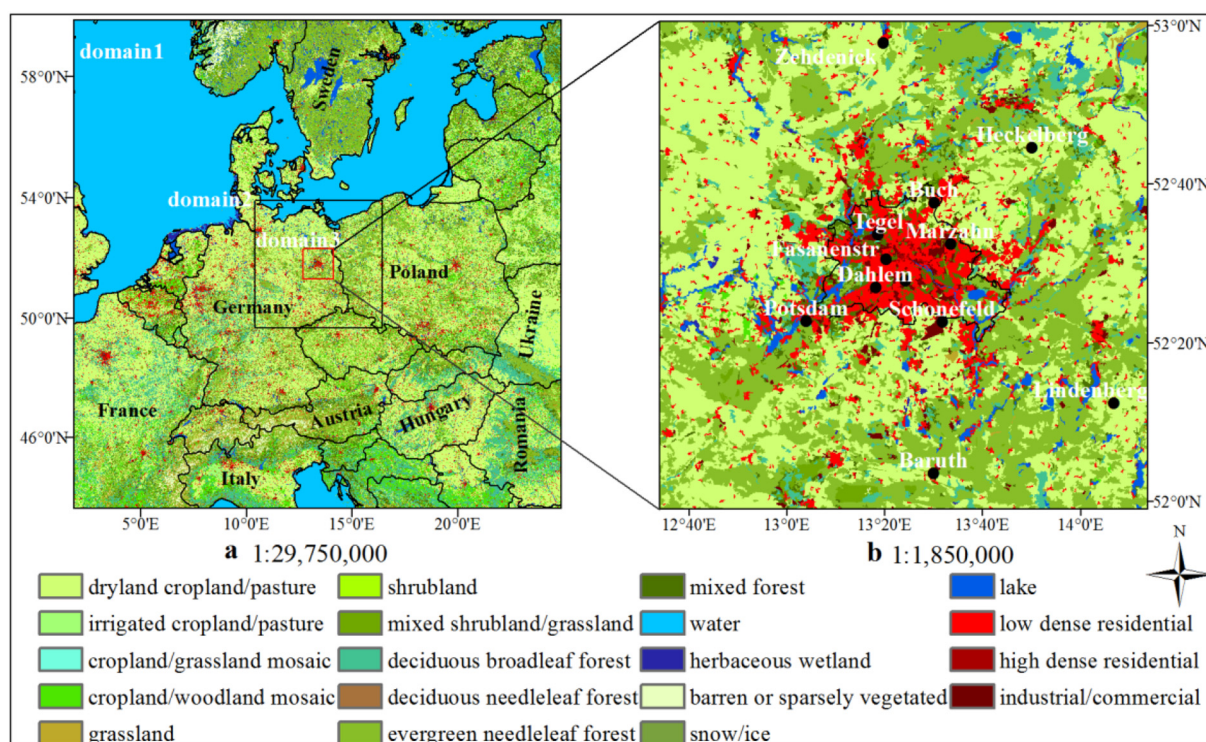


Fig. 1. Setup of (a) the nested domains and (b) the innermost domain. The background shows CORINE land cover. The black points in subplot (b) show the locations of the in-situ observation stations.

were used. The physical parameterization schemes were chosen as follows: (1) the Lin scheme (Lin et al., 1983) for microphysics; (2) the Dudhia (Dudhia, 1989) and RRTM scheme (Mlawer et al., 1997) for shortwave and longwave radiation, respectively; (3) the Eta similarity scheme (Janjic, 1994) for surface layer; (4) the Bougeault–Lacarrère planetary boundary layer scheme (Jänicke et al., 2017); and (5) the Noah LSM scheme (Tewari et al., 2004) for land surface process over natural land cover and the UCM for urban surface process.

2.2.3. Update of urban parameters in the UCM

The critical parameters of UCM (Loridan et al., 2010), including morphological parameters, imperviousness of urban land cover, anthropogenic heat emissions, optical parameters, and thermal parameters, were updated for Berlin by using multi-source datasets. In the UCM, the city is represented as a combination of roofs, walls, and roads and is characterized by the size of the buildings and roads. These morphological parameters were calculated by using the virtual 3D city model datasets from the Department for Urban Development of Berlin Senate (Krüger and Kolbe, 2012). The mean building height ($Height_{building}$, m) and building width ($Width_{building}$, m) were calculated as the sum of the product of the height

of each building and its area weight and the sum of the product of the width of each building and its area weight, respectively. The mean road width ($Width_{road}$, m) was calculated as the sum of the product of the width of each road and its area weight. In the UCM, the urban land cover includes impervious and vegetation components. The impervious component is characterized by the parameter of the fraction of the urban landscape which does not have vegetation (FRC_URB). The FRC_URB was calculated by using the product of imperviousness (ISA_{Copernicus}) version 2012 at a 100 m resolution from Copernicus Land Monitoring Service Pan-European Component (Sannier et al., 2016). The value of FRC_URB was calculated as the mean ISA_{Copernicus} at urban land cover areas. Anthropogenic heat emissions (AHE) were calculated by using a global anthropogenic heat flux database with a high spatial resolution of 30 s and a temporal resolution of 1 h from Dong et al. (2017). The value of AHE was calculated as the mean anthropogenic heat flux at urban land cover areas. The optical parameters (albedo and emissivity) and thermal parameters (thermal conductivity and capacity) of roofs, walls, and roads were determined by referring to the studies of Schubert and Grossman-Clarke (2013) and Wolter (2016), respectively. The updated urban parameters are listed in Table 1.

Table 1
Updated urban parameters in the UCM.

Urban parameters	Objects	Unit	Low dense residential	High dense residential	Industrial/commercial
$Height_{building}$	Building	m	10.27	17.86	10.88
$Width_{building}$	Building	m	16.61	22.83	48.29
$Width_{road}$	Road	m	13.52	16.85	16.28
Albedo & emissivity	Roof	–	0.163 & 0.90		
	Wall	–	0.162 & 0.90		
	Road	–	0.162 & 0.95		
Thermal conductivity & heat capacity	Roof	$J\ m^{-1}\ s^{-1}\ K^{-1}$	$0.695\ \&\ 0.8 \times 10^{-6}$		
	Wall	$\&\ J\ m^{-3}\ K^{-1}$	$0.695\ \&\ 0.8 \times 10^{-6}$		
	Road	–	$0.4004\ \&\ 1.0 \times 10^{-6}$		
FRC_URB	–	–	0.47	0.88	0.78
AHE (July)	–	W/m ²	11.25	37.93	9.95

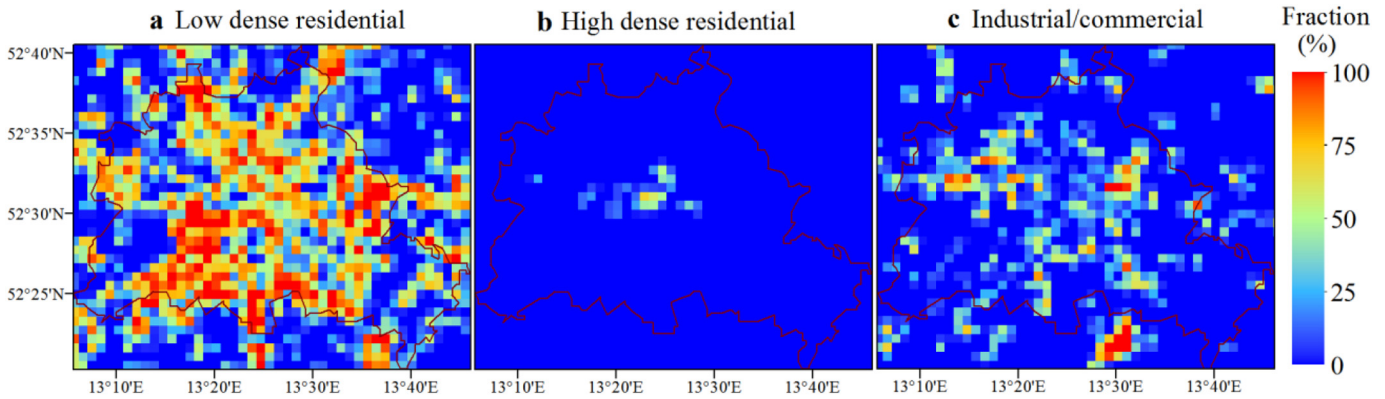


Fig. 2. Spatial patterns of the fractions of (a) low dense residential, (b) high dense residential and (c) industrial/commercial.

2.2.4. Datasets of land cover, initial and lateral boundary conditions

The United States Geological Survey (USGS) land cover classification system with three categories of urban land cover, including low dense residential, high dense residential, and industrial/commercial, was adopted in WRF/UCM. This study used CORINE land cover (CLC) data version 2012 at a 100 m resolution to drive the land surface process in the model. The CLC data was reclassified to the USGS classification system referring to the study of Pineda et al. (2004) and Tewari et al. (2007). The spatial resolution of CLC data is much finer than that of the grids in the domain 3. In order to distinguish the sub-grid variation of the land cover within the domain grids, the mosaic approach of Noah LSM was implemented in this study (Li et al., 2013). The mosaic approach considers more categories of land cover within each grid cell based on the choice of the user. The energy balance in each sub-grid land cover tile is calculated, separately. The mosaic approach helps the model to simulate land surface process more detailed and to avoid the simulation errors from the interpolation of land cover data. In this study, the maximum categories of land cover ($N = 9$) in the grids across domain 3 was set. Fig. 2 shows the spatial patterns of the fraction of the three categories of urban land cover within each grid. The low dense residential occupies a large number of grids with high fractions in the urban areas and several grids with low fractions in the surrounding rural areas. The high dense residential only occupies few grids concentrated in the urban center. The industrial/commercial areas are mainly located in the urban center and airport. The numbers of the grids that are dominated by the urban land cover (fraction > 50%) of low dense residential, high dense residential, and industrial/commercial are 542, 2, and 82, respectively.

Reanalysis data of Global Forecast System (GFS) developed by the National Centers for Environmental Prediction (NCEP) at a 0.5-degree spatial resolution and a 6 hour temporal resolution were applied as the initial and lateral boundary conditions for the model running. In addition, given the long-term running, the daily Real-Time Global Sea Surface Temperature data from NCEP at a 0.5-degree spatial resolution was applied to drive model running.

2.2.5. Simulation period

The period from 21st June to 3rd July 2010 was chosen to carry out the simulation. During this period, clear sky and calm wind situations were dominant. The cloud fraction was less than one quarter during the half of the period. The mean wind speed was 2.46 and 1.81 m/s for the daytime and nighttime, respectively. As recommended by the user's guide of WRF, 6 times of the grid resolution of domain 1 (in km) was set as the time-step (90 s). The hourly simulation data in domain 3 were used to analyze the UHI. The first 24 h were taken as spin-up time and were excluded during the post-processing and analysis of the simulation data.

2.2.6. Model evaluation

The simulated air temperature was evaluated by comparing against the in-situ observation data at twelve meteorological stations (Fig. 1b). Six stations (Tempelhof, Fassanenstr, Buch, Tegel, Dahlem, and Marzahn) are located in the urban areas, and six stations (Heckelberg, Lindenberg, Zehdenick, Baruth, Potsdam, and Schoenefeld) are located in the surrounding rural areas. Statistical indicators, including root mean square error (RMSE), mean bias (MB), Pearson correlation coefficient (r) and Interobserver Agreement (IOA) were used to evaluate the model performance. The equations of these statistical indicators refer to the study of H. Li et al. (2017).

2.3. Calculation of UHI

The air temperature at 2 m height (T_{2m}) in the WRF/UCM is calculated based on the transfer function of sensible heat flux (Li and Bou-Zeid, 2014; Giannaros et al., 2018) as follows

$$T_{2m} = T_s - \frac{SH}{\rho C_{h2m} U_{2m}} \quad (1)$$

where T_s is the surface temperature; SH is the sensible heat flux; C_{h2m} is the transfer coefficient; U_{2m} is the wind speed at 2 m height. The urban land cover includes both impervious and vegetation components. In the UCM, the fractions of impervious and vegetation components are FRC_URB and $(1-FRC_URB)$, respectively. The overall T_s and SH over urban land cover are calculated as the weighted sum of those two variables of impervious and vegetation components as follows

$$T_s = FRC_URB \times T_{s(impervious)} + (1-FRC_URB) \times T_{s(vegetation)} \quad (2)$$

$$SH = FRC_URB \times SH_{(impervious)} + (1-FRC_URB) \times SH_{(vegetation)} \quad (3)$$

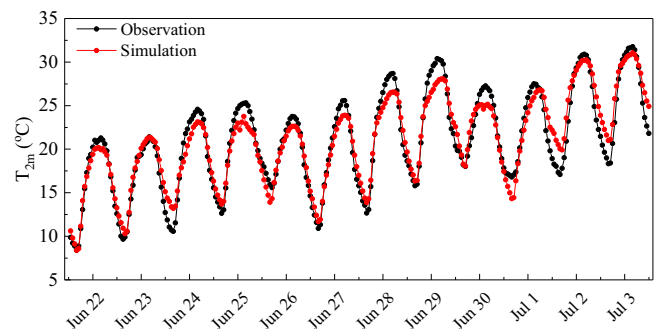


Fig. 3. Comparison of the simulated and observed mean T_{2m} over all in-situ stations.

Table 2
RMSE, MB, r, and IOA of the simulated T_{2m} against the in-situ observations.

Stations	RMSE (°C)	MB (°C)	r	IOA
Overall	1.76	0.02	0.95	0.64
Urban stations	1.83	−0.11	0.94	0.60
Rural stations	1.70	0.15	0.96	0.67

where $T_{s(\text{impervious})}$ and $T_{s(\text{vegetation})}$ are the surface temperature and $SH_{(\text{impervious})}$ and $SH_{(\text{vegetation})}$ are the sensible heat flux of impervious and vegetation components, respectively. Replacing the T_s and SH in Eq. (1) with Eqs. (2) and (3), the equation of T_{2m} over urban land cover is changed to a new form as follows.

$$T_{2m} = FRC_URB \times \left(T_{s(\text{impervious})} - T_{s(\text{vegetation})} - \frac{SH_{(\text{impervious})} - SH_{(\text{vegetation})}}{\rho C_{h2m} U_{2m}} \right) + T_{s(\text{vegetation})} - \frac{SH_{(\text{vegetation})}}{\rho C_{h2m} U_{2m}} \quad (4)$$

The calculation function of T_{2m} becomes a linear function that is fitted using FRC_URB as the variable. The intercept of the function is the air temperature over the vegetation surface, $T_{2m(\text{vegetation})}$. The slope of the function represents the increase in the T_{2m} along with the increase in FRC_URB from 0 (vegetation surface) to 100% (impervious surface) and can be taken as UHII. The mosaic approach enables each grid to include both urban and non-urban land cover tiles (Li et al., 2013). Given that most of the non-urban surface is covered by vegetation in the study area, the land cover of each grid is composed of the impervious component from urban tiles and the vegetation components from urban tiles and non-urban tiles. Thus, the calculation function of T_{2m} becomes a function of the overall ISA_{WRF} at each grid, which is the weighted sum of the individual imperviousness and the corresponding fraction of the three categories of urban land cover tiles within the grid. The ISA_{WRF} is calculated as follows

$$ISA_{WRF} = \sum_{i=31}^{33} FRC_URB(i) \times LANDUSEF(i) \times 100\% \quad (5)$$

where $LANDUSEF(i)$ is the area fraction of low dense residential, high dense residential, and commercial/industrial, whose index (i) in the USGS land cover system are 31, 32, and 33, respectively. The data of $LANDUSEF(i)$ was extracted from the output file of the WRF Preprocessing System program.

The analysis above provides a theoretical basis for the application of the ISA_{WRF} -based function of simulated T_{2m} to quantify UHII. Urban areas have highly inhomogeneous surface. The configuration of land cover categories within each grid vary greatly across the study areas.

As a result, the simulated T_{2m} at the grids with the same ISA_{WRF} may show some differences, due to the different land cover configurations among the grids. In addition, the difference of the reanalysis data at the four latent boundaries may also generate some differences of the simulated T_{2m} among the grids at different locations in the domain. In order to achieve good ISA_{WRF} -based functions of T_{2m} , a zonal analysis method was used. All the grids in the study area were divided into 50 groups with a constant ISA_{WRF} interval of 2%. The first group contains the grids with the ISA_{WRF} ranging from 0 to 2%, and the second group contains the grids with the ISA_{WRF} ranging from 2% to 4%, and so forth until the last group contains the grids with the ISA_{WRF} ranging from 98% to 100%. The mean T_{2m} and ISA_{WRF} were calculated within each group. Then the ISA_{WRF} -based linear functions of the mean simulated T_{2m} were fitted using the mean values of all the groups. Referring to the previous studies (e.g. Oke, 1973), the UHI intensity was defined as the maximum urban-rural difference of temperature in this study. Given that the largest ISA_{WRF} in the study area is smaller than 100% (based on the results in Section 3.2 below), the real UHII is calculated as the products of the slope of the fitted functions and the largest ISA_{WRF} . The coefficient of determination (R^2) was used to evaluate the feasibility of the fitted functions. Water bodies are usually cooler in the daytime and warmer at nighttime than the other land cover, weakening the T_{2m} - ISA_{WRF} relationship. During the calculation of UHII, the grids with water tiles were excluded. The analysis was conducted over three time periods of the day, including daytime, nighttime, and the transition between daytime and nighttime. The daytime (7:00–17:00 UTC) refers to the hours with solar radiation and downward ground heat flux. The nighttime (21:00–03:00 UTC) refers to the hours without solar radiation. The transition period (4:00–6:00 & 18:00–20:00 UTC) refers to the hours with solar radiation, but upward ground heat flux.

3. Results

3.1. Model performance in simulating T_{2m}

In general, the simulated T_{2m} matches the observations in the diurnal cycle well (Fig. 3), with a correlation coefficient of 0.95 ($P < 0.01$). The RMSE and IOA are 1.76 °C and 0.64, respectively (Table 2). The simulation shows an underestimation during the daytime, while an overestimation at nighttime. The mean bias is small, with a value of 0.02 °C. The simulation at the urban stations shows slightly larger errors, compared to the simulation at the rural stations. The model performance is broadly consistent with the previous study in this region for long-term running (Jänicke et al., 2017) and the case studies in other regions (Bhati and Mohan, 2016). Additionally, the large biases mainly happen when the temperatures change significantly. The model running was driven by the lateral boundary condition (reanalysis data). The

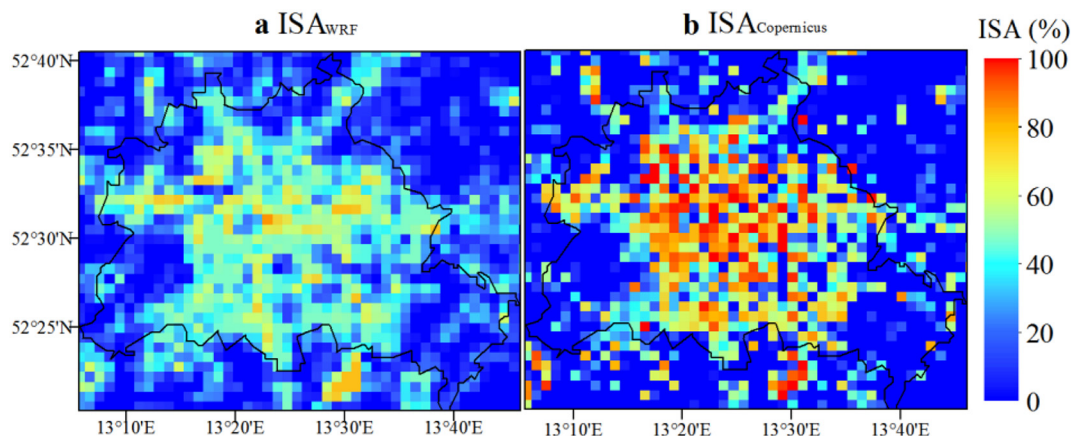


Fig. 4. Spatial patterns of (a) ISA_{WRF} and (b) $ISA_{Copernicus}$.

systematic errors of the reanalysis data in capturing the change of weather processes may be the reason for the large simulation biases during the period with a large change of temperatures (Huang and Gao, 2018). The performance of the model at each station refers to Fig. S1 in the Supplementary file.

3.2. Spatial patterns of ISA_{WRF} and $ISA_{Copernicus}$

Both derived ISA_{WRF} and observed $ISA_{Copernicus}$ are high in the urban areas and low in the surrounding rural areas (Fig. 4). The spatial patterns of the ISA_{WRF} and $ISA_{Copernicus}$ are similar, with a correlation coefficient of 0.74 ($P < 0.01$). But the ISA_{WRF} shows less spatial variation than the $ISA_{Copernicus}$. Compared to the observed $ISA_{Copernicus}$, the ISA_{WRF} is lower in the urban center and higher in the rural areas. The FRC_URB in Eq. (5) was calculated as the mean $ISA_{Copernicus}$ of the three categories of urban land cover in the whole study area. Thus, the derived ISA_{WRF} underestimates the $ISA_{Copernicus}$ in the high impervious areas, while it overestimates the $ISA_{Copernicus}$ in the low impervious areas. This may be one reason for the underestimation of the T_{2m} at the urban stations and the overestimation at the rural stations, as shown in Table 2. The largest ISA_{WRF} (84.97%) is $<100\%$. The spatial pattern of the ISA_{WRF} is

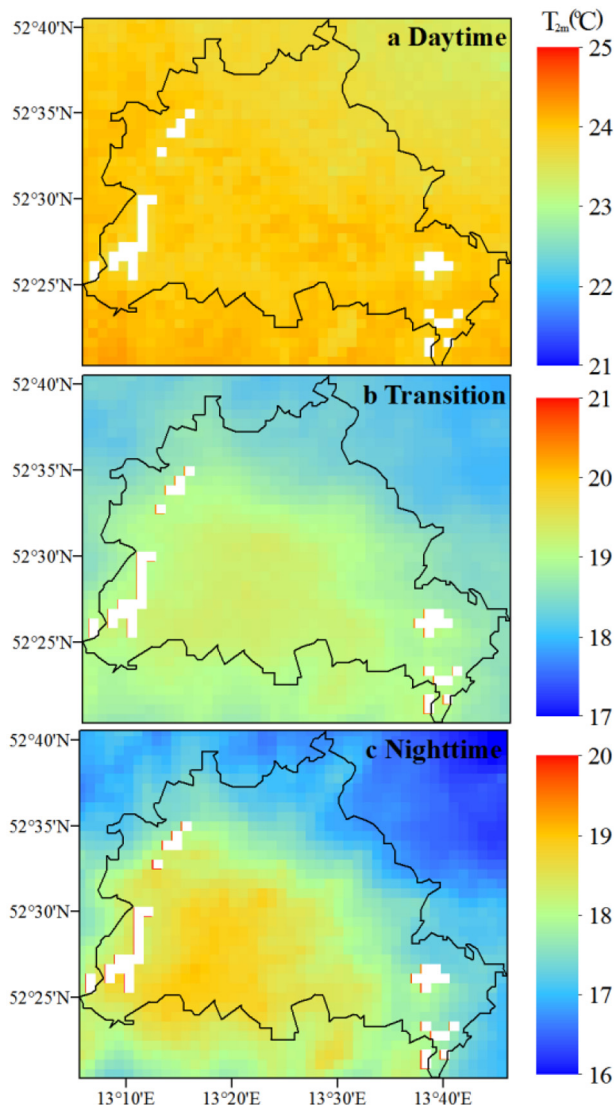


Fig. 5. Spatial patterns of the simulated mean T_{2m} in the (a) daytime, (b) transition period, and (c) nighttime. Grids in white are areas covered by lakes.

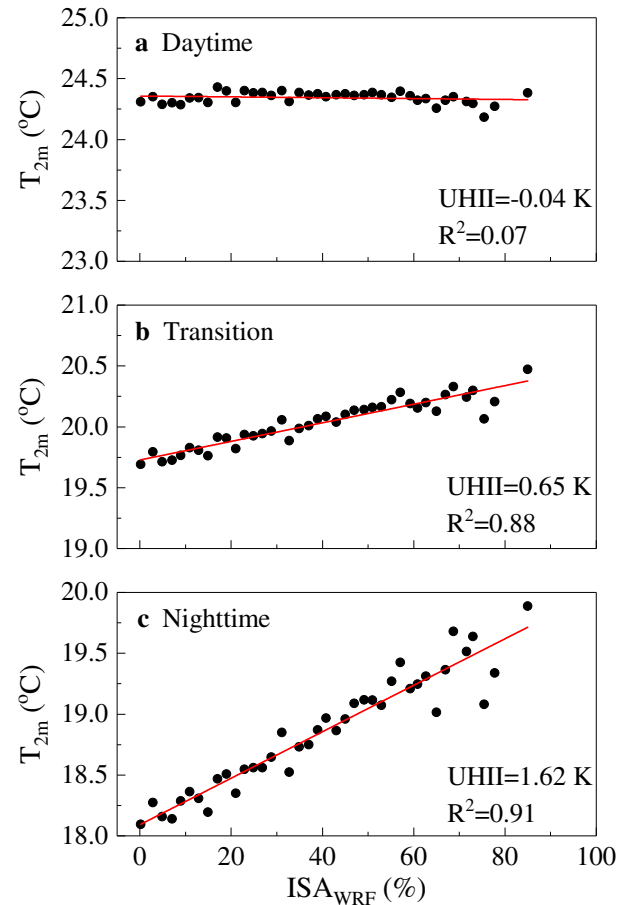


Fig. 6. The relationship between the simulated mean T_{2m} and the ISA_{WRF} in the (a) daytime, (b) transition period, and (c) nighttime during the simulation period. The dots show the mean values of the simulated T_{2m} and ISA_{WRF} within all the 2% intervals of the ISA_{WRF} in the study area.

controlled by the FRC_URB of the three categories of urban land cover. The low ISA_{WRF} is mainly consistent with the low dense residential land cover (Fig. 2a), while the high ISA_{WRF} is mainly corresponding to high dense residential and industrial/commercial land cover (Fig. 2b and c).

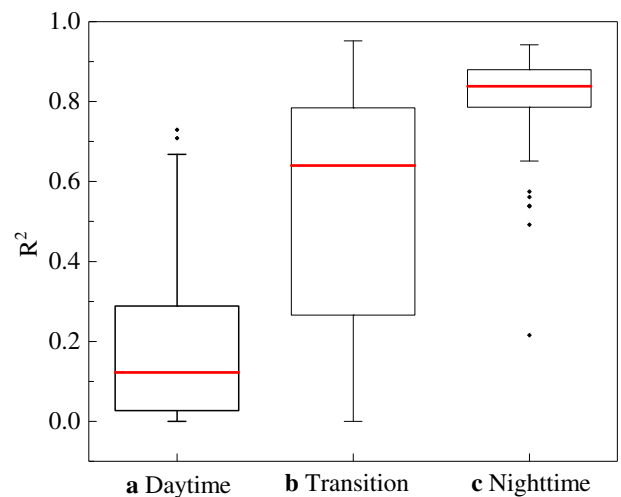


Fig. 7. Box plots of the R^2 for the ISA_{WRF} -based functions of T_{2m} in the (a) daytime, (b) transition period, and (c) nighttime.

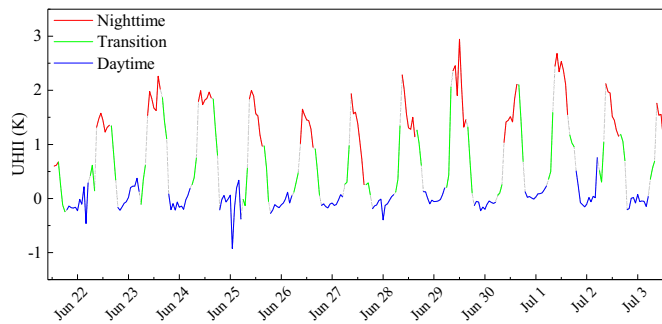


Fig. 8. Diurnal variations of the derived UHII during the simulation period.

3.3. Spatial patterns of simulated T_{2m}

The study area shows a UHI in the nighttime and transition period, with high simulated T_{2m} in the urban areas and low simulated T_{2m} in the surrounding rural areas (Fig. 5). Especially at night, the UHI is pronounced. The spatial pattern of the UHI shows some similarity with that of the ISA_{WRF} as shown in Fig. 4a. In the daytime, the simulated T_{2m} does not show a significant urban-rural difference. The simulated T_{2m} in some of the urban areas is even slightly lower than that in the rural areas. The results are consistent with the study of Jänicke et al. (2017) in this region.

3.4. Quantifying UHII using ISA_{WRF} -based functions of T_{2m}

In the nighttime and the transition period, the mean T_{2m} increases with the increase in the ISA_{WRF} (Fig. 6), presenting positive linear relationships between them. Two linear functions of the mean T_{2m} are well fitted using the ISA_{WRF} , with the R^2 of 0.91 ($P < 0.01$) for the nighttime and 0.88 ($P < 0.01$) for the transition period. The derived UHII is 1.62 K at nighttime and 0.65 K in the transition period, respectively. In the daytime, the T_{2m} - ISA_{WRF} relationship is not significant. The simulated daytime mean T_{2m} generally shows a minor variation with the increase in the ISA_{WRF} . The derived daytime UHII is -0.04 K.

The ISA_{WRF} -based functions of the simulated T_{2m} were also fitted at each hour during the simulation period. At night, most of the functions are well fitted, with $>75\%$ of the R^2 larger than 0.8 (Fig. 7). In the transition period, most of the fitted functions achieve large R^2 with half of values larger than 0.6. In the daytime, the correlation between the simulated T_{2m} and ISA_{WRF} is not high, because of the minor urban-rural difference of the simulated temperature. The derived UHII is high

in the nighttime and low in the daytime, presenting 'U-shaped' curves (Fig. 8). The daily highest UHII usually appears within the 3 h after the sunset. During the daytime, the UHII are slightly negative sometimes from 7:00 to 17:00 UTC. The precipitation can affect the T_{2m} - ISA_{WRF} relationship, subsequently changing the derived UHII. On June 25, the slight precipitation leads to extreme low UHII.

4. Discussion

4.1. Comparison with traditional calculation methods of UHII

In order to further evaluate the new method of the ISA_{WRF} -based function of T_{2m} in quantifying UHII, a comparison between the derived UHII by using the new method and those by using traditional methods was carried out. Traditionally, the difference of the air temperature between selected urban grids and rural grids was defined as UHII. However, the criterions for the selection of urban and rural grids vary. Here we chose three frequently used traditional methods to conduct the comparison study. Referring to the studies of Hamdi and Schayes (2008), Schwarz et al. (2011) and Zhou et al. (2017), the UHII was calculated using the mean temperatures of the grids in the dense urban areas and in the rural areas outside the city. We refer it as traditional method 1. Referring to the studies of Atkinson (2003), Zhao et al. (2014), and Cao et al. (2016), the UHII was calculated using the mean temperatures of the selected urban grids in the city center and of the selected rural grids in the four directions of the surrounding areas. We refer it as traditional method 2. Referring to the studies of Imhoff et al. (2010) and Zhang et al. (2012), the UHII was calculated using the mean temperature of the grids in urban and rural areas as defined by ISA. We refer it as traditional method 3. In this study, the urban center areas within the ring subway (red zone) and the rural areas outside the border (green zone) in Fig. 9 were selected for the calculation of method 1. The nine grids (3×3) in the urban center (square with yellow crossing) and thirty-six ($3 \times 3 \times 4$) grids in the rural areas (squares with yellow slashes) in the four directions of the urban center (Fig. 9) were selected for the calculation of method 2. The grids with ISA_{WRF} larger than 0.7 and the grids with ISA_{WRF} equal to 0 were selected for the calculation of method 3.

The derived UHII using four methods shows similar diurnal variations, with large values at nighttime and small values during the daytime (Fig. 10). The derived UHII using the new method shows a good agreement with the derived UHII using the traditional methods. The correlation coefficients between the derived UHII of the new method and the results of the three traditional methods are 0.97, 0.93, and 0.97 ($P < 0.01$), respectively. However, the derived UHII using the new method is unique for

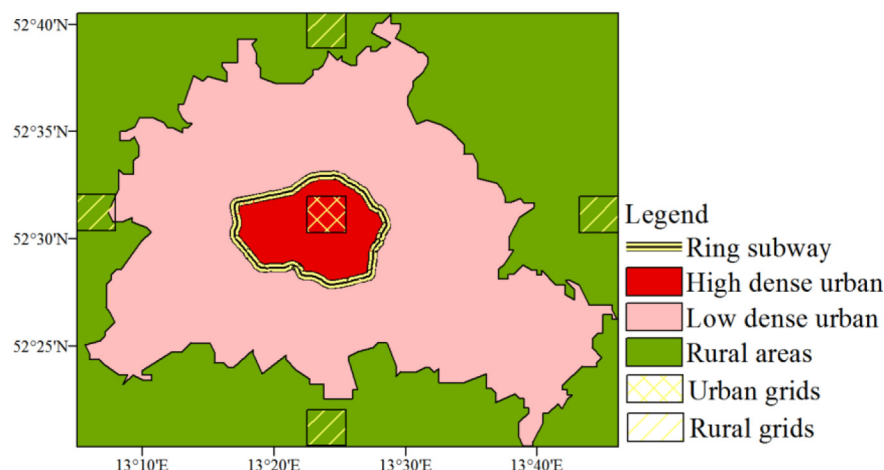


Fig. 9. The location of the selected grids for the calculation of UHII using traditional methods.

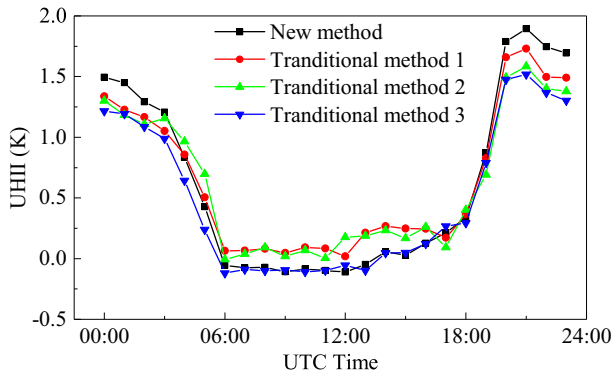


Fig. 10. Diurnal variations of the UHII that is calculated using the new method and three traditional methods.

each city, while the derived UHII using the traditional methods varies with the different selections of urban and rural grids. The new method overcomes the uncertainties from the different selections of urban and rural grids. Moreover, the new method considers the simulated T_{2m} of all the grids in the study area and reflects the overall characteristic of the simulated urban thermal environment, while the traditional methods only consider the T_{2m} of the selected grids (Stewart and Oke, 2012). The derived UHII using the new method shows larger absolute values of UHII than those using the traditional methods (Fig. 10). The ISA_{WRF} -based function of the simulated T_{2m} is a promising approach for the quantification of UHII using WRF/UCM modelling data.

4.2. Physical mechanism that controls the derived UHII

The simulated T_{2m} at each grid is mainly determined by the difference of the T_s and SH between impervious surface and vegetation surface and the ISA_{WRF} , referring to Eq. (4). Usually, the impervious surface shows higher T_s and SH than the vegetation surface, due to lower Bowen ratio and larger energy storage (Oke, 1982; Rizwan et al., 2008). The increasing trends of T_s and SH with the increase in ISA_{WRF} reflect the difference of T_s and SH between impervious surface and vegetation surface. In order to

investigate the physical mechanism that controls the T_{2m} - ISA_{WRF} relationship and the derived UHII in WRF/UCM, the relationships between the simulated T_s and SH and the ISA_{WRF} were examined. In the nighttime and transition period, both the T_s and SH increase linearly with the increase in the ISA_{WRF} (Fig. 11b, c, e, and f). The difference of the T_s and SH between impervious surface and vegetation surface is similar at all grids, leading to the good nighttime and transition - period T_{2m} - ISA_{WRF} relationship. However, in the daytime, the increasing trend of the daytime T_s and SH become larger when the ISA_{WRF} exceeds around 50% (Fig. 11a and d). This two-phase increase reflects the various differences of the T_s and SH between impervious surface and vegetation surface among the grids, which lead to the weak daytime T_{2m} - ISA_{WRF} relationship.

The shading of the buildings could possibly be the main reason for the daytime two-phase increasing trend of the T_s and SH along with the increase in the ISA_{WRF} in the daytime. In the UCM, the T_s and SH of the impervious surface are jointly determined by the energy balance on the roofs, walls, and roads (Tewari et al., 2007; Chen et al., 2011). The daytime incoming radiation on the roads and walls is affected by the shading of the buildings. The low dense residential and high dense residential land cover have the smallest ratio of roof width to road width and the largest ratio of building height to road width (Table 3), respectively, while the industrial/commercial land cover has the largest ratio of roof width to road width and the smallest ratio of building height to road width. The industrial/commercial land cover is less affected by the shading of the buildings, resulting in the larger T_s and SH, compared to the low dense residential and high dense residential land cover. The major urban land cover of the grids with $ISA_{WRF} > 50\%$ is the industrial/commercial land cover, while the major urban land cover of the grids with $ISA_{WRF} < 50\%$ is the low dense residential land cover (Figs. 2 and 4). Therefore, the increasing trend is more significant when the ISA_{WRF} is larger than 50%. The shading-induced two-phase increase in the T_s and SH with the increase in the ISA_{WRF} indicates that the differences of the T_s and SH between impervious surface and vegetation surface among the grids with different urban land cover are inconsistent. As a result, the overall daytime T_{2m} - ISA_{WRF} relationship is weak. In the transition period, the surface energy balance is also affected by the shading of the buildings. However, this influence is limited because of the weak solar radiation and the release of stored heat in the impervious surface during this period. Thus, the increasing trends of T_s

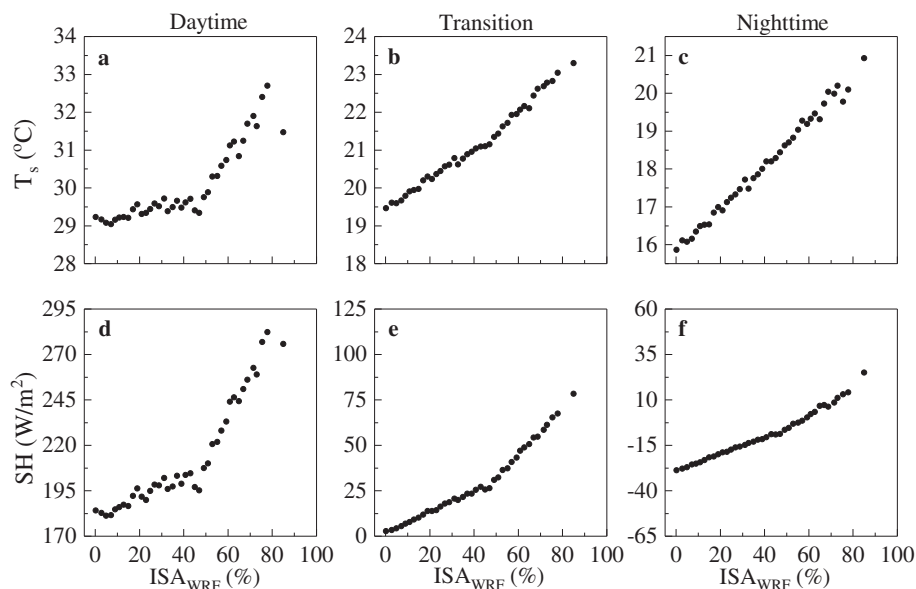


Fig. 11. Variations of the simulated mean (a–c) T_s and (d–f) SH versus mean ISA_{WRF} in the different time periods of the day during the simulation period. Three columns represent the variations in the (left) daytime, (middle) transition period, and (right) nighttime. The dots in each subplot show the simulated mean T_s and SH within all the 2% intervals of the ISA_{WRF} in the study area.

Table 3

The ratio of building height to road width, and the ratio of roof width to road width in the three categories of urban land cover.

Urban land cover variables	Low dense residential	High dense residential	Industrial/commercial
Ratio of building height to road width	0.76	1.06	0.67
Ratio of roof width to road width	0.55	0.58	0.75

and SH do not change significantly with the increase in the ISA_{WRF} (Fig. 11b and e).

The overall difference of the T_s and SH between the impervious surface and the vegetation surface determines the derived UHII, based on Eq. (4). The increasing ranges of the T_s and SH are 3.65, 3.82, and 5.06 K and 100.98, 75.75, and 53.78 W/m² for the daytime, transition period, and nighttime, respectively (Fig. 11). There is a large overall difference of the T_s and a small overall difference of SH between impervious surface and vegetation surface at night, while a small overall difference of the T_s and a large overall difference of the SH between impervious surface and vegetation surface during the day. The former led to the high nighttime UHII, while the latter led to the low and even negative daytime UHII.

This study mainly focuses on the influence of urban geographic information on the urban surface process and UHI and examined its physical mechanisms. The development of convection can affect the heat flux, subsequently changing near-surface UHI. In order to further examine the comprehensive influencing mechanism of UHI, the influence of the development of convection on the simulated UHI needs to be investigated in the further study.

4.3. The influence of specifying urban parameters on the simulation of UHI

Specifying key urban parameters is a big challenge for the simulation of UHI using WRF/UCM (Chen et al., 2011). The current model applies a table lookup method to specify the urban parameters of each grid. In this method, the constant urban parameters are associated with urban land use types. Each parameter only has three values, corresponding to the three types of urban land in the UCM. However, the urban surface has high heterogeneity. The constant urban parameters of limited types of urban land use cannot fully reflect the detailed actual information of urban canopy (Lin et al., 2016). As is shown in Fig. 4, although the overall spatial pattern of the imperviousness is achieved, the derived ISA_{WRF} is lower than the observation in the urban center, while is higher than the observation in the surrounding rural areas, which leads to the under- and overestimation of the temperature in urban and rural areas, respectively. As a result, the derived UHII may be lower than the actual value. Similar problems also exist for other key parameters, such as anthropogenic heat emissions, which also plays an important role for the UHI (Ryu and Baik, 2012). Accurate simulation of UHI needs to input more detailed urban canopy information. The gridded urban parameter datasets may be a good solution. For example, the National Urban Database and Access Portal Tool provides accurate gridded datasets of urban parameters for the cities in the United States, which can contribute to the improvement of WRF/UCM performance (Ching et al., 2009). In northern Taiwan, Lin et al. (2016) modified the UCM by incorporating 2-D spatial distribution maps of urban fraction and anthropogenic heat and generated a better simulation result. Future study could consider establishing the gridded urban parameter datasets for more cities if robust urban datasets are available.

5. Conclusions

This study simulated UHI in the city of Berlin using WRF/UCM and quantified the UHII using the method of ISA_{WRF} -based functions of the simulated T_{2m} . The model performed well in simulating T_{2m} during the study period. The correlation coefficient and RMSE between the simulation and the observation were 0.95 ($P < 0.01$) and 1.76 °C,

respectively. The simulation results showed a pronounced UHI at nighttime in the study area. The simulated nighttime T_{2m} linearly increased with the increase in the ISA_{WRF} . The ISA_{WRF} -based linear functions of T_{2m} were well fitted. The derived UHII showed 'U-shaped' diurnal variations, with large values at nighttime. The daytime UHII was low and even negative. The differences of the simulated T_s and SH between impervious surface and vegetation surface jointly controlled the derived UHII. In the nighttime, the large difference of T_s and small difference of SH between impervious surface and vegetation surface generated high nighttime UHII and vice versa in the daytime. The new method overcomes the uncertainties of traditional methods in selecting urban/rural grids and considers the overall characteristic of the simulated UHI at all the grids in the study area.

However, there are still some uncertainties and improvement space for the current simulation and quantification method. As for the simulation of temperature, the current WRF/UCM used a table-based method to input the urban parameters of the three types of urban land cover. The problems of under- and overestimation of the simulation exist because of the difference of the constant urban parameters and actual various values. Future simulation should consider applying the gridded urban parameters to drive model running if the robust datasets are available. As for the quantification of the UHII, this study used horizontal imperviousness to fit the function of temperature, referring to the calculation equations of temperature in the model. The vertical imperviousness associated with the wall may also have some influence on the simulated temperature. Future study should take this influence into consideration, despite the influence is thought to be complicated. Meanwhile, it should be noted that some functions in the daytime were not well fitted, because of the rather small urban-rural difference of the simulated daytime temperature. The derived UHII based on these fitted functions may have some uncertainties. It is better to check the magnitude and diurnal variation of the derived UHII carefully to avoid the possible incorrect values. Additionally, it should be noted that the good performance of the new method in estimating UHII was achieved under typical UHI conditions with the calm and cloudless weather. Under other weather conditions, the dependence of temperature on ISA may become weak. The feasibility of the application of the new method under other weather conditions needs further evaluation in the future study.

Supplementary data to this article can be found online at <https://doi.org/10.1016/j.scitotenv.2018.10.025>.

Acknowledgments

This research is supported by the China Scholarship Council. The authors thank the Beijing Office of Freie Universität Berlin. Special thanks go to Patricia Margerison for proofreading this manuscript.

References

- American Association for the Advancement of Science (AAAS), 2016. *Rise of the city. Science* 352, 906–907.
- Atkinson, B.W., 2003. Numerical modelling of urban heat-island intensity. *Bound.-Layer Meteorol.* 109, 285–310.
- Bhati, S., Mohan, M., 2016. WRF model evaluation for the urban heat island assessment under varying land use/land cover and reference site conditions. *Theor. Appl. Climatol.* 126, 385–400.
- Cao, C., Lee, X., Liu, S., Schultz, N., Xiao, W., Zhang, M., Zhao, L., 2016. Urban heat islands in China enhanced by haze pollution. *Nat. Commun.* 7. <https://doi.org/10.1038/ncomms12509>.
- Chen, F., Kusaka, H., Bornstein, R., Ching, J., Grimmond, C.S.B., Grossman-Clarke, S., Loran, T., Manning, K.W., Martilli, A., Miao, S., Sailor, D., Salamanca, F.P., Taha, H.,

- Tewari, M., Wang, X., Wyszogrodzki, A.A., Zhang, C., 2011. The integrated WRF/urban modelling system: development, evaluation, and applications to urban environmental problems. *Int. J. Climatol.* 31, 273–288.
- Ching, J., Brown, M., McPherson, T., Burian, S., Chen, F., Cionco, R., Hanna, A., Hultgren, T., Sailor, D., Taha, H., Williams, D., 2009. National urban database and access portal tool. *Bull. Am. Meteorol. Soc.* 90 (8), 1157–1168.
- Dong, Y., Varquez, A.C.G., Kanda, M., 2017. Global anthropogenic heat flux database with high spatial resolution. *Atmos. Environ.* 150, 276–294.
- Dudhia, J., 1989. Numerical study of convection observed during the Winter Monsoon Experiment using a mesoscale two-dimensional model. *J. Atmos. Sci.* 46, 3077–3107.
- Giannaros, C., Nenes, A., Giannaros, T.M., Kourtidis, K., Melas, D., 2018. A comprehensive approach for the simulation of the Urban Heat Island effect with the WRF/SLUCM modeling system: the case of Athens (Greece). *Atmos. Res.* 201, 86–101.
- Hamdi, R., Schayes, G., 2008. Sensitivity study of the urban heat island intensity to urban characteristics. *Int. J. Climatol.* 28 (7), 973–982.
- Huang, D., Gao, S., 2018. Impact of different reanalysis data on WRF dynamical downscaling over China. *Atmos. Res.* 200, 25–35.
- Imhoff, M.L., Zhang, P., Wolfe, R.E., Bounoua, L., 2010. Remote sensing of the urban heat island effect across biomes in the continental USA. *Remote Sens. Environ.* 114 (3), 504–513.
- Jacobs, S.J., Gallant, A.J., Tapper, N.J., Li, D., 2018. Use of cool roofs and vegetation to mitigate urban heat and improve human thermal stress in Melbourne, Australia. *J. Appl. Meteorol. Climatol.* <https://doi.org/10.1175/JAMC-D-17-0243.1>.
- Jänicke, B., Meier, F., Fenner, D., Fehrenbach, U., Holtmann, A., Scherer, D., 2017. Urban-rural differences in near-surface air temperature as resolved by the Central Europe Refined analysis (CER): sensitivity to planetary boundary layer schemes and urban canopy models. *Int. J. Climatol.* 37 (4), 2063–2079.
- Janjic, Z.I., 1994. The step-mountain Eta coordinate model: further developments of the convection, viscous sublayer and turbulence closure schemes. *Mon. Weather Rev.* 122, 927–945.
- Kottmeier, C., Biegert, C., Corsmeier, U., 2007. Effects of urban land use on surface temperature in Berlin: case study. *J. Urban Plann. Dev.* 133 (2), 128–137.
- Krüger, A., Kolbe, T.H., 2012. Building analysis for urban energy planning using key indicators on virtual 3D city models—the energy atlas of Berlin. *Int. Arch. Photogramm. Remote. Sens. Spat. Inf. Sci.* 39 (B2), 145–150.
- Kusaka, H., Kimura, F., 2004. Coupling a single-layer urban canopy model with a simple atmospheric model: impact on urban heat island simulation for an idealized case. *J. Appl. Meteorol.* 43, 1899–1910.
- Kusaka, H., Kondo, H., Kikigawa, Y., Kimura, F., 2001. A simple single-layer urban canopy model for atmospheric models: comparison with multi-layer and slab models. *Bound.-Layer Meteorol.* 101 (3), 329–358.
- Kusaka, H., Chen, F., Tewari, M., Hirakuchi, H., 2005. Impact of using the urban canopy model on the simulation of the heat island. WRF/MM5 users' workshop. Boulder, Colorado. Session 4.2. <http://www2.mmm.ucar.edu/wrf/users/workshops/WS2005/abstracts/Session4/2-Kusaka.pdf>.
- Kusaka, H., Hara, M., Takane, Y., 2012. Urban climate projection by the WRF model at 3-km horizontal grid increment: dynamical downscaling and predicting heat stress in the 2070's August for Tokyo, Osaka, and Nagoya metropolises. *J. Meteorol. Soc. Jpn.* 90, 47–63.
- Li, D., Bou-Zeid, E., 2014. Quality and sensitivity of high-resolution numerical simulation of urban heat islands. *Environ. Res. Lett.* 9 (5), 055001.
- Li, D., Bou-Zeid, E., Barlage, M., Chen, F., Smith, J.A., 2013. Development and evaluation of a mosaic approach in the WRF-Noah framework. *J. Geophys. Res. Atmos.* 118, 918–935.
- Li, H., Wolter, M., Wang, X., Sodoudi, S., 2017. Impact of land cover data on the simulation of urban heat island for Berlin using WRF coupled with bulk approach of Noah-LSM. *Theor. Appl. Climatol.* <https://doi.org/10.1007/s00704-017-2253-z>.
- Li, X., Zhou, Y., Asrar, G.R., Imhoff, M., Li, X., 2017. The surface urban heat island response to urban expansion: a panel analysis for the conterminous United States. *Sci. Total Environ.* 605, 426–435.
- Li, H., Zhou, Y., Li, X., Meng, L., Wang, X., Wu, S., Sodoudi, S., 2018a. A new method to quantify surface urban heat island intensity. *Sci. Total Environ.* 624, 262–272.
- Li, H., Meier, F., Lee, X., Chakraborty, T., Liu, J., Schaap, M., Sodoudi, S., 2018b. Interaction between urban heat island and urban pollution island during summer in Berlin. *Sci. Total Environ.* 636, 818–828.
- Lin, Y., Richard, D.F., Harold, D.O., 1983. Bulk parameterization of the snow field in a cloud model. *J. Clim. Appl. Meteorol.* 22, 1065–1092.
- Lin, C.Y., Su, C.J., Kusaka, H., Akimoto, Y., Sheng, Y.F., Huang, J.C., Hsu, H.H., 2016. Impact of an improved WRF urban canopy model on diurnal air temperature simulation over northern Taiwan. *Atmos. Chem. Phys.* 16, 1809–1822.
- Loridan, T., Grimmond, C.S.B., Grossman-Clarke, S., Chen, F., Tewari, M., Manning, K., Martilli, A., Kusaka, H., Best, M., 2010. Trade-offs and responsiveness of the single-layer urban canopy parametrization in WRF: an offline evaluation using the MOSCEM optimization algorithm and field observations. *Q. J. R. Meteorol. Soc.* 136 (649), 997–1019.
- Meehl, G.A., Tebaldi, C., 2004. More intense, more frequent, and longer lasting heat waves in the 21st century. *Science* 305, 994–997.
- Miao, S., Chen, F., LeMone, M.A., Tewari, M., Li, Q., Wang, Y., 2009. An observational and modeling study of characteristics of urban heat island and boundary layer structures in Beijing. *J. Appl. Meteorol. Climatol.* 48 (3), 484–501.
- Mirzaei, P.A., Haghighat, F., 2010. Approaches to study urban heat island—abilities and limitations. *Build. Environ.* 45 (10), 2192–2201.
- Mlawer, E.J., Steven, J.T., Patrick, D.B., Iacono, M.J., Clough, S.A., 1997. Radiative transfer for inhomogeneous atmospheres: RRTM, a validated correlated-k model for the longwave. *J. Geophys. Res.* 102, 16663–16682.
- Oke, T.R., 1973. City size and the urban heat island. *Atmos. Environ.* 7, 769–779.
- Oke, T.R., 1982. The energetic basis of the urban heat island. *Q. J. R. Meteorol. Soc.* 108 (455), 1–24.
- Phelan, P.E., Kaloush, K., Miner, M., Golden, J., Phelan, B., Silva, H., Taylor, R.A., 2015. Urban heat island: mechanisms, implications, and possible remedies. *Annu. Rev. Environ. Resour.* 40, 285–307.
- Pineda, N., Jorba, O., Jorge, J., Baldasano, J., 2004. Using NOAA AVHRR and SPOT VGT data to estimate surface parameters: application to a mesoscale meteorological model. *Int. J. Remote Sens.* 25, 129–143.
- Rizwan, A.M., Dennis, L.Y.C., Liu, C., 2008. A review on the generation, determination and mitigation of Urban Heat Island. *J. Environ. Sci.* 20, 120–128.
- Ryu, Y.H., Baik, J.J., 2012. Quantitative analysis of factors contributing to urban heat island intensity. *J. Appl. Meteorol. Climatol.* 51 (5), 842–854.
- Salamanca, F., Martilli, A., Yagüe, C., 2012. A numerical study of the Urban Heat Island over Madrid during the DESIREX (2008) campaign with WRF and an evaluation of simple mitigation strategies. *Int. J. Climatol.* 32 (15), 2372–2386.
- San José, R., Pérez, J.L., González, R.M., 2013. Very high resolution urban simulations with WRF/UCM and CMAQ over European cities. *Urban Environment*. Springer, Dordrecht, pp. 293–301.
- Sannier, C., Gallego, J., Dahmer, J., Smith, G., Dufourmont, H., Pennec, A., 2016. Validation of Copernicus high resolution layer on imperviousness degree for 2006, 2009 and 2012. Proceedings of the International Symposium on Spatial Accuracy Assessment in Natural Resources and Environmental Sciences, Montpellier, France, pp. 5–8.
- Schatz, J., Kucharik, C.J., 2014. Seasonality of the urban heat island effect in Madison, Wisconsin. *J. Appl. Meteorol. Climatol.* 53 (10), 2371–2386.
- Schatz, J., Kucharik, C.J., 2015. Urban climate effects on extreme temperatures in Madison, Wisconsin, USA. *Environ. Res. Lett.* 10 (9), 094024.
- Schubert, S., Grossman-Clarke, S., 2013. The influence of green areas and roof albedos on air temperatures during Extreme Heat Events in Berlin, Germany. *Meteorol. Z.* 22 (2), 131–143.
- Schwarz, N., Lautenbach, S., Seppelt, R., 2011. Exploring indicators for quantifying surface urban heat islands of European cities with MODIS land surface temperatures. *Remote Sens. Environ.* 115 (12), 3175–3186.
- Stewart, I.D., 2011. A systematic review and scientific critique of methodology in modern urban heat island literature. *Int. J. Climatol.* 31 (2), 200–217.
- Stewart, I.D., Oke, T.R., 2012. Local climate zones for urban temperature studies. *Bull. Am. Meteorol. Soc.* 93 (12), 1879–1900.
- Tan, J., Zheng, Y., Tang, X., Guo, C., Li, L., Song, G., Zhen, X., Yuan, D., Kalkstein, A.J., Li, F., Chen, H., 2010. The urban heat island and its impact on heat waves and human health in Shanghai. *Int. J. Climatol.* 30 (1), 75–84.
- Tewari, M., Chen, F., Wang, W., Dudhia, J., LeMone, M.A., Mitchell, K., Ek, M., Gayno, G., Wegiel, J., Cuenca, R.H., 2004. Implementation and verification of the unified Noah land surface model in the WRF model. 20th Conference on Weather Analysis and Forecasting/16th Conference on Numerical Weather Prediction, pp. 11–15.
- Tewari, M., Chen, F., Kusaka, H., Miao, S., 2007. Coupled WRF/Unified Noah/urban-canopy modeling system. NCAR WRF Documentation. NCAR, Boulder, p. 122. <http://citeseerx.ist.psu.edu/viewdoc/download?doi=10.1.1.468.3545&rep=rep1&type=pdf>.
- Vahmani, P., Hogue, T.S., 2015. Urban irrigation effects on WRF-UCM summertime forecast skill over the Los Angeles metropolitan area. *J. Geophys. Res. Atmos.* 120 (19), 9869–9881.
- Wolter, M., 2016. Implementierung und Anpassung des WRF-Modells für Berlin & projektbezogene Ableitung der Straßenoberflächentemperatur. (Master thesis). Freie Universität, Berlin, Germany.
- Yang, X., Leung, L.R., Zhao, N., Zhao, C., Qian, Y., Hu, K., Liu, X., Chen, B., 2017. Contribution of urbanization to the increase of extreme heat events in an urban agglomeration in east China. *Geophys. Res. Lett.* <https://doi.org/10.1002/2017GL074084>.
- Zauri, R., Schiaroli, R., Leonardi, F.G., Berni, N., 2010. Numerical weather prediction models' temperature post-processing in heat wave early warning in Umbria: a case study and preliminary results. *Ital. J. Agrometeorol.* 15 (3), 43–60.
- Zhang, P., Imhoff, M.L., Wolfe, R.E., Bounoua, L., 2010. Characterizing urban heat islands of global settlements using MODIS and nighttime lights products. *Can. J. Remote Sens.* 36 (3), 185–196.
- Zhang, P., Imhoff, M.L., Bounoua, L., Wolfe, R.E., 2012. Exploring the influence of impervious surface density and shape on urban heat islands in the northeast United States using MODIS and Landsat. *Can. J. Remote Sens.* 38 (4), 441–451.
- Zhao, L., Lee, X., Smith, R.B., Oleson, K., 2014. Strong contributions of local background climate to urban heat islands. *Nature* 511, 216–219.
- Zhong, S., Qian, Y., Zhao, C., Leung, R., Wang, H., Yang, B., Fan, J., Yan, H., Yang, X., Liu, D., 2017. Urbanization-induced urban heat island and aerosol effects on climate extremes in the Yangtze River Delta region of China. *Atmos. Chem. Phys.* 17 (8), 5439–5457.
- Zhou, B., Rybski, D., Kropp, J.P., 2017. The role of city size and urban form in the surface urban heat island. *Sci. Rep.* 7 (1), 4791.